https://doi.org/10.3311/PPCi.36933



Periodica Polytechnica Civil Engineering

# Experimental Investigation of High-performance Fiber-reinforced Cementitious Composite and its Effect on RC Beams by Numerical Method

Reza Khaleghi[1], Ahmad Shokoohfar[1*], Reza Farokhzad[1], Mehrzad TahamouliRoudsari[2]

[1] Department of Civil Engineering, Qazvin Branch, Islamic Azad University, P. O. B. 34185-1416, 34199-15195 Qazvin, Iran
[2] Department of Civil Engineering, Kermanshah Branch, Islamic Azad University, Imam Khomeini Campus, Farhikhtegan Bld., Shahid J'afari St., 67189-97551 Kermanshah, Iran
[*] Corresponding author, e-mail: ahmad.shokoohfar@qiau.ac.ir

Received: 21 March 2024, Accepted: 16 August 2024, Published online: 27 August 2024

**Abstract**

In the present study, experimental investigations were initially conducted on high-performance fiber-reinforced cementitious composite (HPFRCC). A total of 9 samples were examined and subjected to a 4-point bending test. The sample lengths were standardized at 500 and 1700 mm. The variables under scrutiny included the impact of Micro Steel, Macro Steel, and polyvinyl alcohol fibers. Furthermore, the models were scrutinized under two conditions: with and without glass fiber reinforced polymer (GFRP) bars. The number of samples was 9. In the second part of the article, subsequent to verifying the experimental samples from the current study alongside a concrete beam, numerical analyses were carried out to assess the influence of HPFRCC on the behavior of RC beams. Similarly, the impact of GFRP diameter, as well as the height of HPFRCCs, on the seismic performance of RC beams, was investigated by conducting 36 numerical analyses. The analyses were carried out using nonlinear static methods, with monotonic loading. The model outputs encompass elastic stiffness, ultimate strength, relative stiffness, and energy dissipation. The experimental results showed that the use of macro steel fibers in models without GFRP rebars has better results on the flexural behavior of HPFRCC. Moreover, by reinforcing RC beams with HPFRCC, a 70% increase in energy dissipation was observed. The elastic stiffness and ultimate strength of the strengthened beam are directly proportional to the ratio of the HPFRCC's elastic flexural stiffness to that of the original beam. These results increase proportionally as this ratio rises.

**Keywords**

strengthening, ultra-high performance fiber reinforced, finite element model, RC beam, GFRP bars, experimental test

## 1 Introduction

The improvement and fortification of concrete structures are essential goals in the field of civil engineering. Over recent decades, a multitude of methodologies have been devised to repair and bolster reinforced concrete beams [1, 2]. Such techniques encompass near-surface mounted approaches [3, 4], externally bonded methods [5], utilization of textile-reinforced mortar [6, 7], and application of ultra-high performance concrete layers [8–10].

Numerous numerical and experimental investigations have focused on fortifying concrete beams. Al-Osta et al. [11] investigated two methodologies for reinforcing reinforced concrete (RC) beams with ultra-high performance fiber reinforced concrete (UHPFRC). The first method entailed sandblasting and in-situ casting, while the second involved the use of epoxy adhesive to affix precast UHPFRC strips. Strengthening configurations encompassed reinforcement at the bottom, two longitudinal sides, and three sides. Bond strength tests were conducted for both techniques. The findings revealed favorable enhancements in flexural behavior, particularly notable with three-sided strengthening, showcasing the highest capacity increase. However, concerns arose regarding potential ductility loss associated with increased UHPFRC usage. Notably, finite element and analytical models accurately predicted beam behavior. Naser et al. [12] emphasize the versatility of Fiber-reinforced polymer (FRP) composites in strengthening and retrofitting structures, owing to their exceptional mechanical properties and customizable nature. They advocate for advanced finite element simulations to navigate the intricacies of FRP-strengthened concrete structures, covering adhesive simulation, material properties, and various FRP types/systems under

**Cite this article as:** Khaleghi, R., Shokoohfar, A., Farokhzad, R., TahamouliRoudsari, M. "Experimental Investigation of High-performance Fiber-reinforced Cementitious Composite and its Effect on RC Beams by Numerical Method", Periodica Polytechnica Civil Engineering, 2024. https://doi.org/10.3311/PPCi.36933

diverse loading conditions. Their insights offer valuable guidance for researchers, practitioners, and students alike. Said et al. [13] scrutinize the effectiveness of employing UHPFRC to augment the shear strength of RC beams. Their experimental investigations revealed noteworthy enhancements in shear strength, stiffness, ductility, and toughness when compared to un-strengthened beams. Full casting of UHPFRC and roughened surfaces contribute to enhanced performance. Folino et al. [14] analyze full-scale reinforced concrete beams with fiber-reinforced concrete, observing improved post-peak behavior attributed to fibers. Although the tensile strength increased in small samples, there were no significant differences in cracking load values in full-scale beams. Discrepancies emerged in predicting bending and shear strength compared to international recommendations. Abadel et al. [15] investigate the effectiveness of shear stirrups and carbon fiber-reinforced plastic (CFRP) strengthening in bolstering the shear strength of deep beams. Shear stirrups improved shear strength, whereas the UHPFRC mix increased strength and deformation capacity. Bui et al.'s [16] study, conducted an experimental study on the shear performance of concrete beams reinforced with steel fibers, excluding the use of stirrups. Zhang et al. [17] investigated how adding basalt fiber–reinforced polymer sheets affect the behavior of reinforced concrete beams that lack stirrups. Yu et al. [18] applied artificial intelligence to assess the shear capacity of steel fiber reinforced concrete beams without stirrups. Alshboul et al. [19] developed a predictive model using machine learning to estimate the shear strength of slender reinforced concrete beams, also without stirrups. In the research on prediction models for compressive mechanical properties of steel fiber-reinforced cementitious composites [20], the focus was on developing models to predict the compressive behavior of these composites. The study on constitutive models for ultra-high performance concrete under true tri-axial compression and fiber-reinforced polymer-confined ultra-high performance concrete [21] aimed to create models that describe the behavior of this concrete under complex loading conditions and confinement. Additionally, the investigation into stress-strain models for ultra-high performance concrete and ultra-high performance fiber-reinforced concrete under triaxial compression [22] concentrated on developing models to characterize the stress-strain responses of these materials under triaxial compression.

The present study commenced with experimental investigations aimed at assessing the influence of steel fibers and glass fiber reinforced polymer (GFRP) rebars on the bending performance of HPFRCC. To this end, a 4-point bending test was conducted on nine samples, each with lengths of 500 and 1700 mm, respectively. The steel fibers comprised Micro Steel, recycled polyethylene terephthalate, and polyvinyl alcohol. The experimental studies yielded force-displacement diagrams as outputs. In the subsequent phase of the research, numerical validation was performed on a concrete beam alongside nine experimental models from the current study. Subsequently, the impact of HPFRCC height and GFRP diameter on displacement diagrams across 18 different cases was investigated. Furthermore, the study delved into the effects of reinforcing RC beams with HPFRCC. Upon calculating force-displacement diagrams for the models, the influence of GFRP height and diameter on concrete beam parameters was examined. The outputs of the parametric model encompassed effective stiffness, ultimate strength, relative stiffness, and energy dissipation. The number of experimental samples was 9, and the number of numerical models was 36. Specifically, 18 models were HPRCC only, and 18 models were beams equipped with HPRCC.

A noteworthy aspect of this work lies in its exploration of the simultaneous utilization of steel fibers and GFRP bars in HPFRCC plates, as well as their effects on pre-existing concrete beams, thus contributing novel insights to the field.

## 2 Experimental programs

In the experimental study section, nine HPFRCC specimens underwent testing in a 4-point bending setup. To enhance the accuracy of the numerical model verification, the models were assessed under two conditions: with and without GFRP bars. Additionally, fibers were incorporated to augment the tensile strength of concrete. The subsequent subsections provide a detailed interpretation of the experimental samples.

### 2.1 Details of samples

The experimental samples examined in this study comprised nine specimens with and without GFRP bars. These samples incorporated three types of fibers in the concrete matrix, namely Micro Steel (MS), Macro Steel fibers (MSH), and polyvinyl alcohol (PVA), as depicted in Fig. 1 (a). The grading curve of the aggregates is shown in Fig. 1 (a). Detailed specifications of these fibers are provided in Table 1. Additionally, Table 1 includes the material parameters for the GFRP bars utilized in the samples.

Dog-bone shaped specimens were used to calculate the tensile strength. The preparation of specimens and testing methods followed the recommendations of the Japan

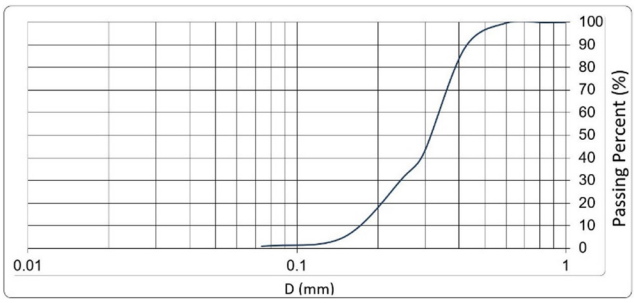


(a)

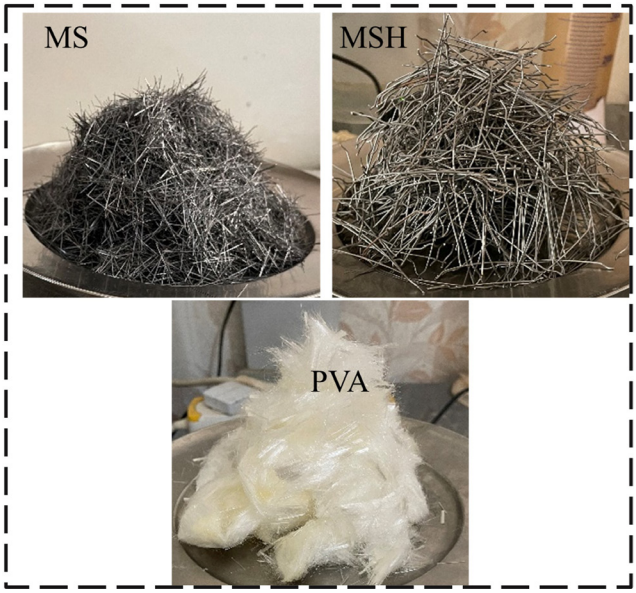


(b)

**Fig. 1** (a) Grading curve of the aggregate (b) The fibers used in the samples

**Table 1** Fiber specifications

| Fibers | Tensile strength (MPa) | Young's modulus (GPa) | Density (g/cm$^3$) | Length (mm) | Diameter (mm) |
|---|---|---|---|---|---|
| MS | 2720 | 210 | 7.85 | 16 | 0.25 |
| MSH | 1120 | 200 | 7.85 | 50 | 0.7 |
| PVA | 1250 | 33 | 1.18 | 12 | $15 \times 10^{-3}$ |
| GFRP ∅6 | 1325 | 52.1 | - | - | 6 |
| GFRP ∅8 | 1251 | 48.2 | - | - | 8 |

Society of Civil Engineers (JSCE) in 2008 [23] as referenced in [24]. For this purpose, steel tensile grips compatible with the specimen dimensions were fabricated, and tensile tests were conducted using a 2-ton capacity servo-electrical universal testing machine, as shown in Fig. 2 (a). A loading rate of 0.5 mm/min was applied, and specimens with dimensions as specified in [24] were used, as shown in Fig. 2 (b).

To ensure uniformity in the concrete materials across all models and accurately assess the effect of fibers, efforts were made to maintain consistent concrete properties.


(a)

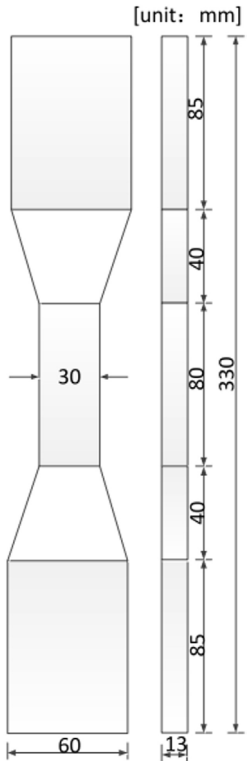


(b)

**Fig. 2** (a) Specimen dimensions and (b) Tensile test equipment for dog-bone shaped specimen

To calculate the compressive strength of concrete, a 10 cm cube mold was used [25]. Similarly, the average compressive strength of samples M1, M2, and M3 was calculated

as 93 MPa, 85.5 MPa, and 92.4 MPa respectively. Fig. 3 (a) illustrates the mold used for casting the samples and the concreting process of the models. Fibers were uniformly added to the samples to ensure even distribution throughout the concrete, as depicted in Fig. 3 (b).

In the fabrication of the samples, Type I Portland cement with a minimum compressive strength of 425 kg/cm$^2$ from the West Kermanshah Cement Factory with a Blaine fineness of 3250 cm$^2$/g was used. Silica fume slurry, a thick gray liquid with a density of 1.35 g/cm$^3$, was employed. Additionally, calcium carbonate ($CaCO_3$) with a density of 2.86 g/cm$^3$ was used. The Quantum superplasticizer, a product of Ramka Building Chemical Industries, known for its high water-reducing and workability-enhancing capabilities, with a density of 1.08 g/cm$^3$, was applied. The mix designs for the high-performance fiber-reinforced cementitious composite are presented in Table 2. In the naming convention, the fiber content is indicated by the percentage, with the corresponding weight shown in the respective row.

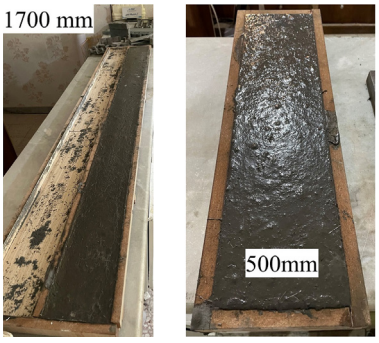


(a)


(b)

**Fig. 3** (a) The mold of 500 and 1700 mm samples (b) Mortar of specimens

**Table 2** Mix designs (kg/m$^3$)

| Mixture series | PC | SF* | $CaCO_3$ | QP | S | W | SP |
|---|---|---|---|---|---|---|---|
| M1 | 1005 | 253 | 28.6 | 42 | 871 | 229 | 30 |
| M2 | 1034 | 252.65 | | 42 | 871 | 239.85 | 36 |
| M3 | 1034 | 252.65 | | 42 | 871 | 239.85 | 32 |

The columns have the following meaning: PC: Portland cement, QP: Quartz powder, S: Sand, W: Water, SP: Superplasticizer, $CaCO_3$: Calcium carbonate, SF*: the dry silica fume content in the silica fume slurry. The water content in the slurry is listed in column W.

To calculate Young's modulus of HPFRCC, the proposed equation from [26] was used, as presented in Eq. (1). In Eq. (1), $f_c$ represents the compressive strength of HPFRCC in MPa. Furthermore, Table 3 provides detailed specifications and dimensions of all models. The second column of Table 3 indicates the distance between two supports or the net length of the beams. Each sample's length exceeded the distance between its two supports by 200 mm. The clear cover of the GFRP bars remained consistent across all samples, set at 7 mm. Fig. 4 presents the cross-section of all models along with their respective dimensions.

$$E = 18000\left(\frac{f_c}{10}\right)^{\left(\frac{1}{3}\right)} \tag{1}$$

Upon reviewing papers [27, 28], it was determined that there is no specific standard for mixing cementitious composite materials. Therefore, the mixing procedure was established experimentally. Sand, silica fume slurry, and

**Table 3** Specifications of all experimental samples

| Sample label | Net length (mm) | GFRP bars | Fibers (%) | | |
|---|---|---|---|---|---|
| | | | MS | PVA | MSH |
| M1-300 | 300 | - | 1.8 | 0.5 | - |
| M1-300-G6 | 300 | 2Ø6 | 1.8 | 0.5 | - |
| M1-1500-G8 | 1500 | 2Ø8 | 1.8 | 0.5 | - |
| M2-300 | 300 | - | 1.5 | 0.5 | - |
| M2-300-G6 | 300 | 2Ø6 | 1.5 | 0.5 | - |
| M2-1500-G6 | 1500 | 2Ø6 | 1.5 | 0.5 | - |
| M3-300 | 300 | - | 1.5 | - | 1 |
| M3-300-G6 | 300 | 2Ø6 | 1.5 | - | 1 |
| M3-1500-G6 | 1500 | 2Ø6 | 1.5 | - | 1 |

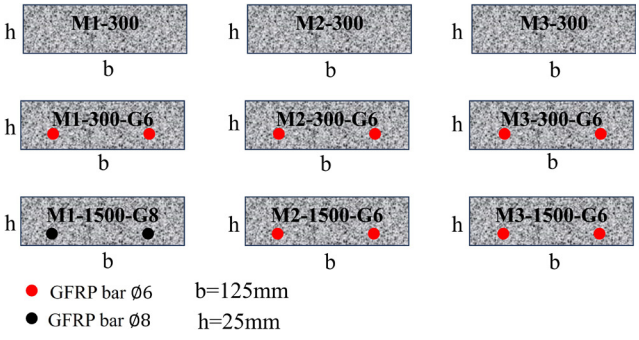


**Fig. 4** The cross-section of experimental samples

superplasticizer were first mixed at low speed for one minute, then at high speed for another minute. Subsequently, non-steel fibers were added to the mixture and mixed at a low speed for two minutes. After adding the cement, the mixing continued at a low speed for another two minutes. The mixing procedure before adding steel fibers adhered to ASTM C305-13 [29] standards using a mixer. After the addition of steel fibers, the mixture was manually stirred for two minutes.

This section outlines the loading procedure applied to the models. The models underwent loading in a 4-point bending configuration, as illustrated in Fig. 5. A linear variable differential transformer (LVDT) was employed to measure the deflection at the sample's midpoint. The loading speed was set at 0.5 mm/min for samples with a length of 500 mm (spanning 300 mm between two supports) and 0.25 N/s [30] for samples with a length of 1700 mm (spanning 1500 mm between supports).

The experimental specimens were subjected to monotonic loading until the models reached the point of failure. Upon analysis, it was noted that the inclusion of steel fibers led to an increase in tensile strength following the appearance of cracks in the tensile section. Fig. 6 depicts the

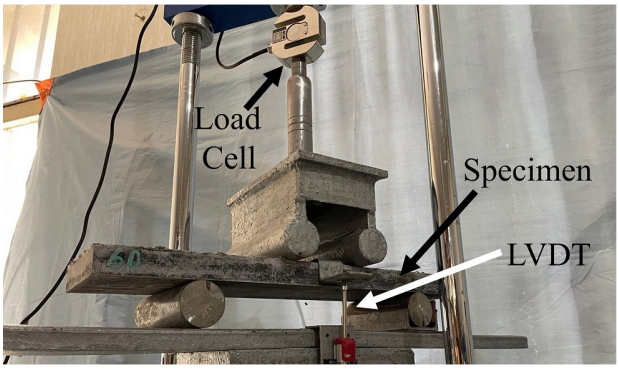


(a)

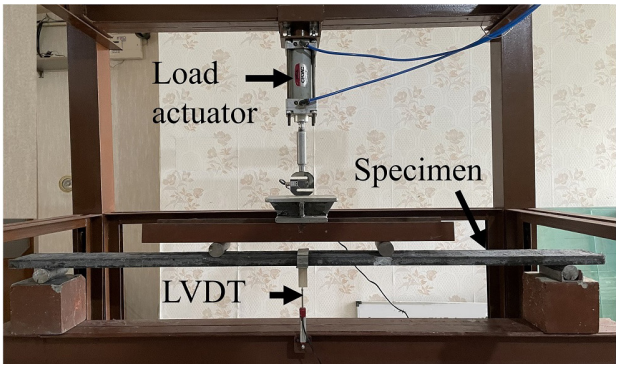


(b)

**Fig. 5** Test setup for models of lengths: (a) 500 mm and (b) 1700 mm

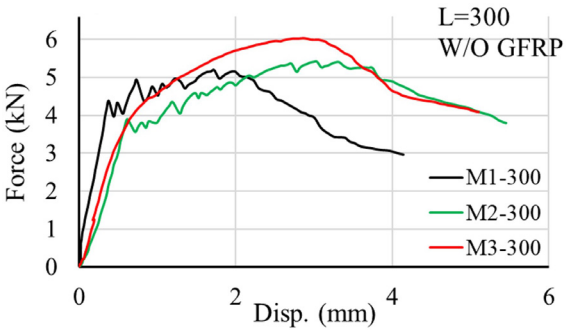


(a)

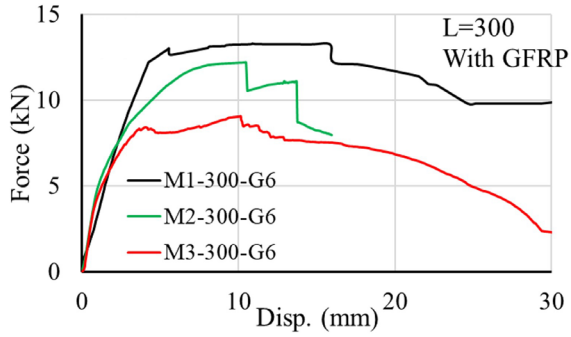


(b)

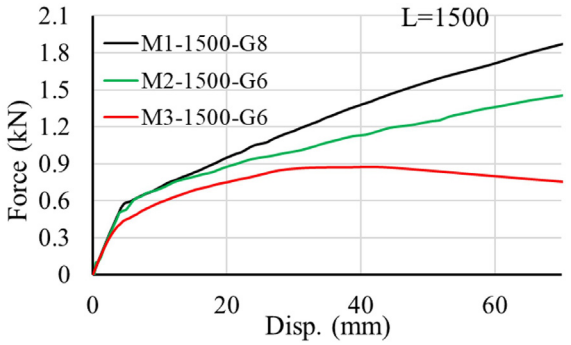


(c)

**Fig. 6** Force-displacement diagrams of models (a) with a length of 300 and without GFRP (b) with a length of 300 and with GFRP (c) with a length of 1500 and with GFRP

force-displacement diagrams of the model results. In these diagrams, the horizontal axis represents the deflection at the midpoint of the samples.

In the models without GFRP rebars (Fig. 6 (a)), all results exhibited a deflection drop to less than 4 mm. Notably, compared to the models lacking GFRP bars, the M1 model experienced an earlier failure. Conversely, in the models with GFRP bars and a length of 300 mm (Fig. 6 (b)), the capacity of the M1 model exceeded that of other models. The outcome of the M3-300-G6 model indicated a deflection of 5 mm, attributed to the initial crack formation in the tensile region. Subsequently, the

steel fibers underwent tension, thereby sustaining the result until reaching a deflection of 16 mm. In contrast, Sample M2-300-G6 exhibited a significant deflection drop of 11 mm due to cracking in its tensile section.

The M1 and M2 models with a length of 1500 mm (Fig. 6 (c)) sustained loading until completion without any discernible drop in results. However, during the fabrication of sample M3-1500-G6, it was observed that employing macro steel fibers with elongated lengths posed challenges for GFRP models with low clear cover. Notably, during the application process, no macro steel fibers were embedded beneath the GFRP rebars. Consequently, the space was reinforced solely with microfiber mortar, resulting in subpar performance compared to the other samples. As depicted in Fig. 6 (c), the capacity curve of the M3-1500-G6 model exhibited a drop at a deflection of 38 mm.

Fig. 7 illustrates the failure of samples lacking GFRP rebars, demonstrating the uniform distribution of steel fibers within the fractured region. Additionally, Fig. 8 displays the M2-1500-G6 model under loading conditions.

In the construction of the specimen, several factors must be considered to enhance its behavior. Given the thinness of these plates, the gap between the GFRP and the underlying surface of the plate is minimal. Consequently, the aggregate size must be selected to ensure that the concrete is appropriately placed beneath the rebar. It should also be ensured that the fibers are uniformly distributed on the surface under the rebars. During the construction of specimens incorporating macro fibers, it was observed that the use of long steel macro fibers is not an effective approach. The steel macro fibers fail to adequately position themselves in the space beneath the rebars during mold placement. As a result, this space is exclusively filled with mortar containing microfibers.

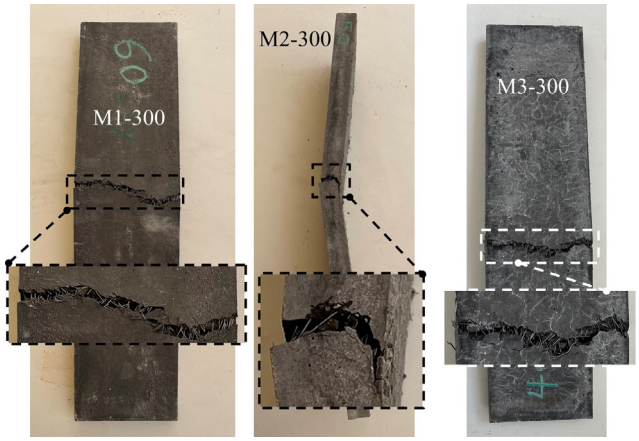


**Fig. 7** The failure of models without GFRP

**Fig. 8** The sample M2-1500-G6 during loading

## 3 Parametric studies

Parametric analysis in this study was conducted using ABAQUS software [31]. Initially, the numerical model underwent verification to ensure precise results. The parametric studies aimed to explore the influence of HPFRCC on RC beams. In addition to validating the experimental samples from the current research, an experimental RC beam sample was also employed to verify the numerical model. Subsequently, the models are verified separately in the following section.

### 3.1 Verification of RC beam

In this section, verification of the RC beam was conducted using the experimental sample provided by Huang et al. [32]. The specifications of this sample are illustrated in Fig. 9, indicating that the test was performed under 4-point bending conditions. The RC beam underwent monotonic loading. The average compressive strength of the concrete sample is recorded as 49.9 MPa. Furthermore, the yield strength and ultimate strength of the longitudinal reinforcements are specified as 386 MPa and 572 MPa, respectively. Similarly, the yield and ultimate strength of the stirrups are noted as 280 MPa and 480 MPa.

In this section, numerical modeling of the experimental sample was carried out. Concrete was modeled using solid elements with eight nodes and 24 translational degrees of freedom, employing reduced integration mode (C3D8R) [33, 34]. The reinforcements were modeled using 2-node linear 3-D truss elements (T3D2), and sliding of concrete and rebars during loading was neglected. The models were analyzed using the Static General solver, with consideration for large deformations. Numerical analyses were conducted using the Newton-Raphson method.

The concrete stress-strain diagram was defined in accordance with Eurocode 2 [35], based on Eq. (2). In Eqs. (3) and (4), two parameters of Eq. (2) are delineated. The parameters for Eqs. (3) and (4) are illustrated in Fig. 10. As per Eurocode 2 recommendations, the values of $\varepsilon_{c1}$ and $\varepsilon_{cu1}$ were specified as 0.0024 and 0.0035, respectively. Additionally, Young's modulus of concrete

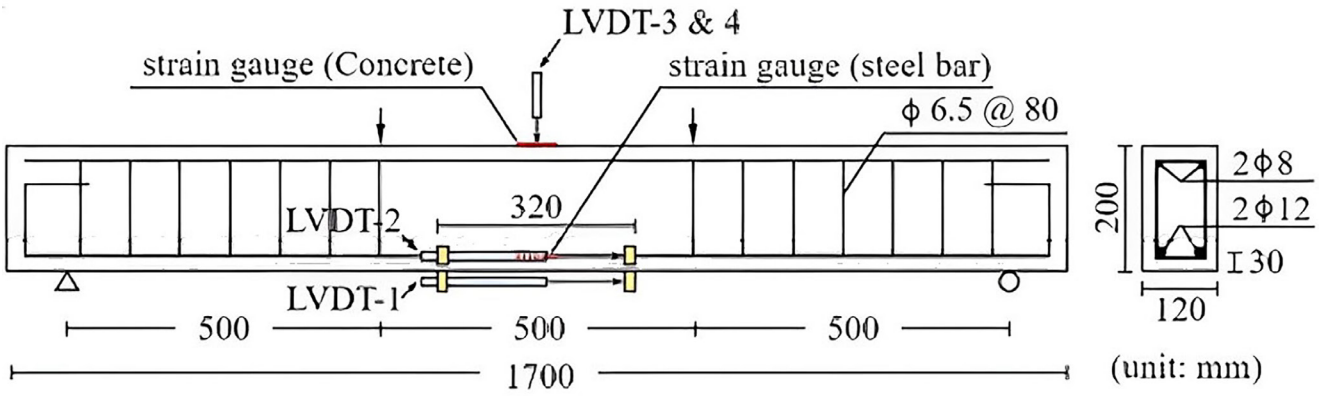


**Fig. 9** Details of the experimental sample [32]

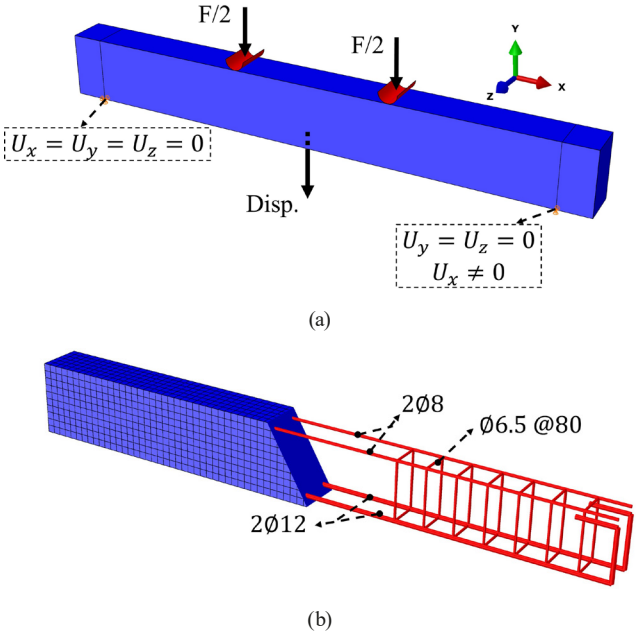


**Fig. 10** (a) Boundary conditions of the numerical model (b) Details of rebars

($E_c$) was set to 37 GPa. The tensile behavior of concrete was assumed to be one-tenth of its compressive behavior. Six mesh sensitivity analyses were conducted to ascertain the optimal mesh dimensions, with the outcomes summarized in Table 4. It was determined that the mesh size of 2 cm yielded the maximum strength across all models, indicating its optimal suitability.

The concrete damage plasticity (CDP) model was employed to simulate concrete failure, with its parameters presented in Table 5 [36]. The material properties of the rebars were defined using a bilinear model, which includes their yield and ultimate stresses [37]. During the analysis, the slip between the rebars and concrete was neglected.

$$\sigma = \frac{\eta(k-\eta)}{1+(k-2)\eta}\sigma_{cu} \tag{2}$$

**Table 4** Results of RC beam sensitivity analysis to mesh dimensions

| Model | Mesh size (cm) | Error (%) $F_{max}$ corresponding to model 4 |
|---|---|---|
| 1 | 8 | 12.21 |
| 2 | 6 | 8.14 |
| 3 | 4 | 3.21 |
| 4 | 2 | 0 |
| 5 | 1 | 0.13 |
| 6 | 0.5 | 0.1 |

**Table 5** Suggested values for CDP [31]

| Dilation angel | Eccentricity | $Fb_0/fc_0$ | $K$ | Viscosity parameter |
|---|---|---|---|---|
| 34 | 0.1 | 0.16 | 0.667 | 0.001 |

$$\eta = \frac{\varepsilon}{\varepsilon_{c1}} \tag{3}$$

$$k = 1.05\frac{E_c\varepsilon_{c1}}{\sigma_{cu}} \tag{4}$$

Concrete damage parameters in compression and tension were defined according to Eqs. (5) and (6), where *t* and *c* denote concrete parameters in tension and compression, respectively. Similarly, $\epsilon^{pl}$ represents the plastic strain, while *b* signifies a constant parameter ranging from 0 to 1.

$$d_c = 1 - \frac{\sigma_{cu}E_c^{-1}}{\epsilon_c^{pl}\left(\frac{1}{b_c}-1\right)+\sigma_{cu}E_c^{-1}} \tag{5}$$

$$d_t = 1 - \frac{\sigma_t E_c^{-1}}{\epsilon_t^{pl}\left(\frac{1}{b_t}-1\right)+\sigma_t E_c^{-1}} \tag{6}$$

Fig. 10 (a) illustrates the location of loading and boundary conditions. Fig. 10 (b) provides the details of the rebars. Upon analysis of the numerical model, its force-displacement

results were compared with those of the experimental model in Fig. 11 (a), revealing close alignment between the two. Furthermore, Fig. 11 (b) presents a comparison between the crack patterns observed in the numerical model and the experimental sample at a yield displacement of 5 mm, highlighting the accurate estimation provided by the numerical model of the experimental crack pattern.

### 3.2 Verification of the HPFRCC

In this section, verification of the experimental samples from the current research was conducted. All nine models outlined in Table 3 were utilized to calibrate the numerical model. Concrete was modeled using an 8-node solid element, and the models were analyzed using the displacement-control technique with the General Static solver in ABAQUS. Numerical analyses were performed using the Newton-Raphson method, with consideration for large deformations to enhance the accuracy of the numerical model [38, 39]. The behavior of GFRP bars was simulated by assuming them as proportionately elastic materials up to rupture [40].

Additionally, the ratio of compressive to tensile strength of GFRP was set at 55% [41]. Based on the sensitivity analysis results, the mesh dimensions of all models (concrete and GFRP bars) were set at 2 cm. Additionally, to enhance the accuracy of the model results for models with varying heights, the meshing of the model in height was carried out in 4 layers. The width of the mesh was kept constant in these cases. This approach was based on a sensitivity analysis, which resulted in optimal mesh dimensions.

Fig. 12 illustrates two examples of these models with lengths of 1700 mm and 500 mm. Fig. 13 compares the experimental and numerical results.

## 4 Parametric studies

### 4.1 Parametric investigation of HPFRCC

The focus of this section lies in the numerical investigation of the impact of GFRP diameter and HPFRCC height on its flexural behavior. Given that these two parameters can be altered in strengthened RC beams, they were treated as variables. The model studied in this section was assumed to have a length of 1700 mm (as per Fig. 12 (a)). Boundary conditions, loading type, and mesh dimensions were established in accordance with Section 3.2. The parametric models introduced in this section are outlined in Table 6. HPFRCC height is considered across three cases: 20 mm, 30 mm, and 40 mm. Additionally, the GFRP diameter is examined across two cases. The force-displacement results of the models listed in Table 6 were analyzed and are presented in Fig. 14. Moreover, the initial slope of the curves, or elastic stiffness, for all models was calculated and compared to the stiffness of the RC beam (19 kN/mm) based on Fig. 11 (a). The results are summarized in Table 6.

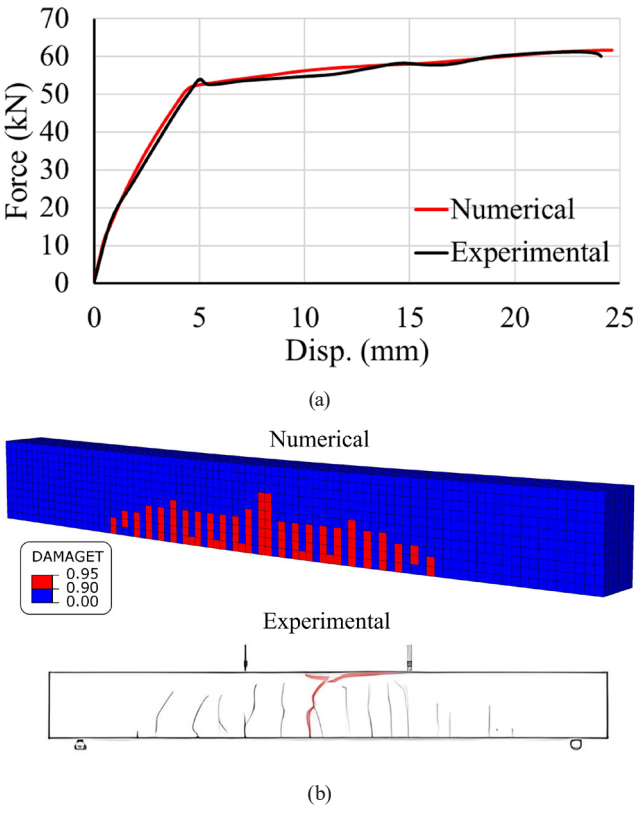


**Fig. 11** Comparison of numerical and experimental results (a) force-displacement (b) cracking pattern

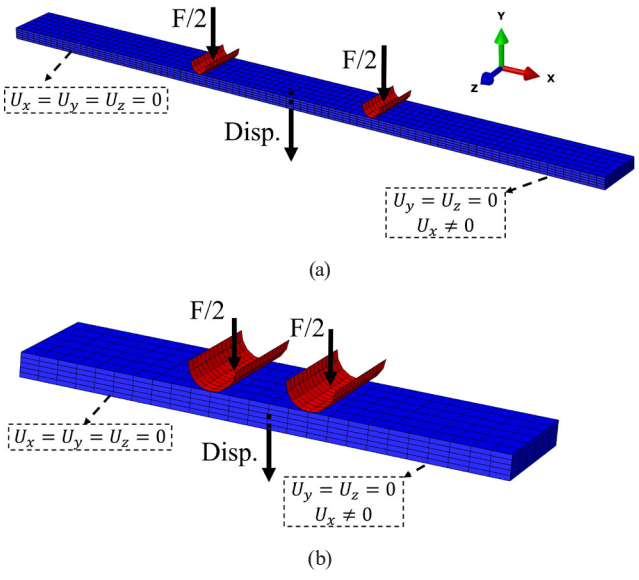


**Fig. 12** Boundary conditions of the meshed models for the length of (a) 1700 mm and (b) 500 mm

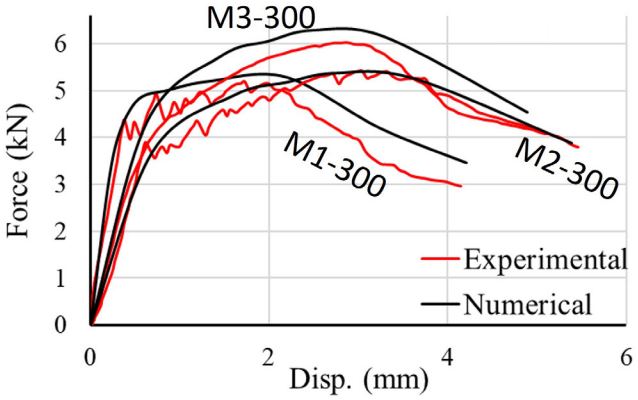


(a)

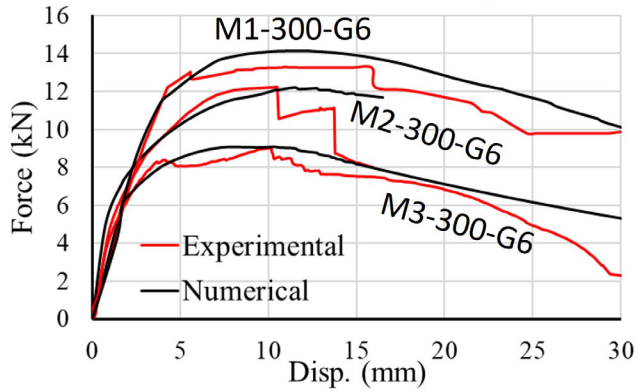


(b)

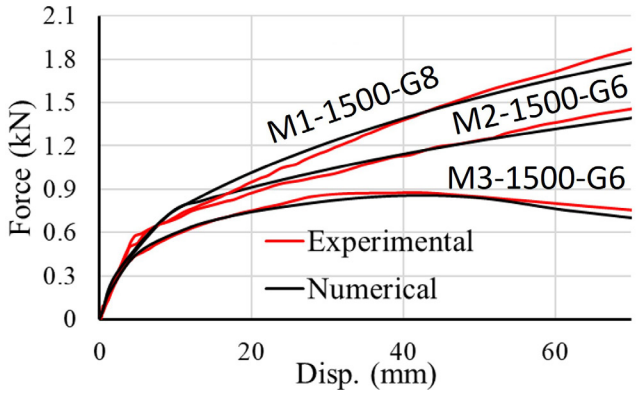


(c)

**Fig. 13** Comparison of numerical and experimental models

### 4.2 Investigation of the strengthened beam

In this section, a parametric analysis was conducted to investigate the strengthened beam. To achieve this, the models listed in Table 6, possessing identical dimensions and specifications but with a length of 1500 mm, were connected to the verified RC beam. Fig. 15 illustrates the parametric model examined in this section. The connection between HPFRCC and the concrete beam was established using a "Tie" constraint [11]. A Tie constraint in ABAQUS is used to bind two surfaces together, ensuring no relative motion occurs between them. To facilitate a comparison between the strengthened beam and the original beam (OB), the model's loading was executed in a manner analogous to the verified beam, utilizing the same maximum displacement. The objective was to analyze the influence of HPFRCC height and GFRP rebar diameter on the parameters of the RC beam.

**Table 6** The list of strengthened beam models

| Models | Model type | GFRP diameter (mm) | HPFRCC height (mm) | $\alpha$ = Normalized stiffness to RC beam (%) |
|---|---|---|---|---|
| M1-0.4 | M1 | 2∅6 | 20 | 0.4 |
| M1-2 | | | 30 | 2 |
| M1-4.72 | | | 40 | 4.72 |
| M1-1.18 | | 2∅8 | 20 | 1.18 |
| M1-2.67 | | | 30 | 2.67 |
| M1-4.8 | | | 40 | 4.8 |
| M2-0.53 | M2 | 2∅6 | 20 | 0.53 |
| M2-1.85 | | | 30 | 1.85 |
| M2-3.6 | | | 40 | 3.6 |
| M2-1.2 | | 2∅8 | 20 | 1.2 |
| M2-2.3 | | | 30 | 2.3 |
| M2-4.18 | | | 40 | 4.18 |
| M3-0.54 | M3 | 2∅6 | 20 | 0.54 |
| M3-1.96 | | | 30 | 1.96 |
| M3-4.64 | | | 40 | 4.64 |
| M3-1 | | 2∅8 | 20 | 1 |
| M3-2.42 | | | 30 | 2.42 |
| M3-4.72 | | | 40 | 4.72 |

Throughout this analysis, the dimensions and specifications of the RC beam remained constant across all models. Additionally, the beam was reinforced with HPFRCC according to the dimensions outlined in Table 6.

After examining the models, the force-displacement results were calculated according to Fig. 16. In Fig. 16, the results of the OB are also shown. As can be seen, the names of strengthened beams are based on the type of HPFRCC (M1, M2, and M3) and the ratio of HPFRCC elastic stiffness to the OB ($\alpha$ according to Table 6).

In this section, two critical parameters, namely the maximum strength and elastic stiffness of the models, are scrutinized. The ultimate strength is defined as the maximum force that the model can resist, representing a fundamental parameter of beams. On the other hand, stiffness is a pivotal characteristic of reinforced concrete structures, signifying their ability to withstand load/displacement. A higher stiffness indicates a reduced displacement experienced by the model under a constant force.

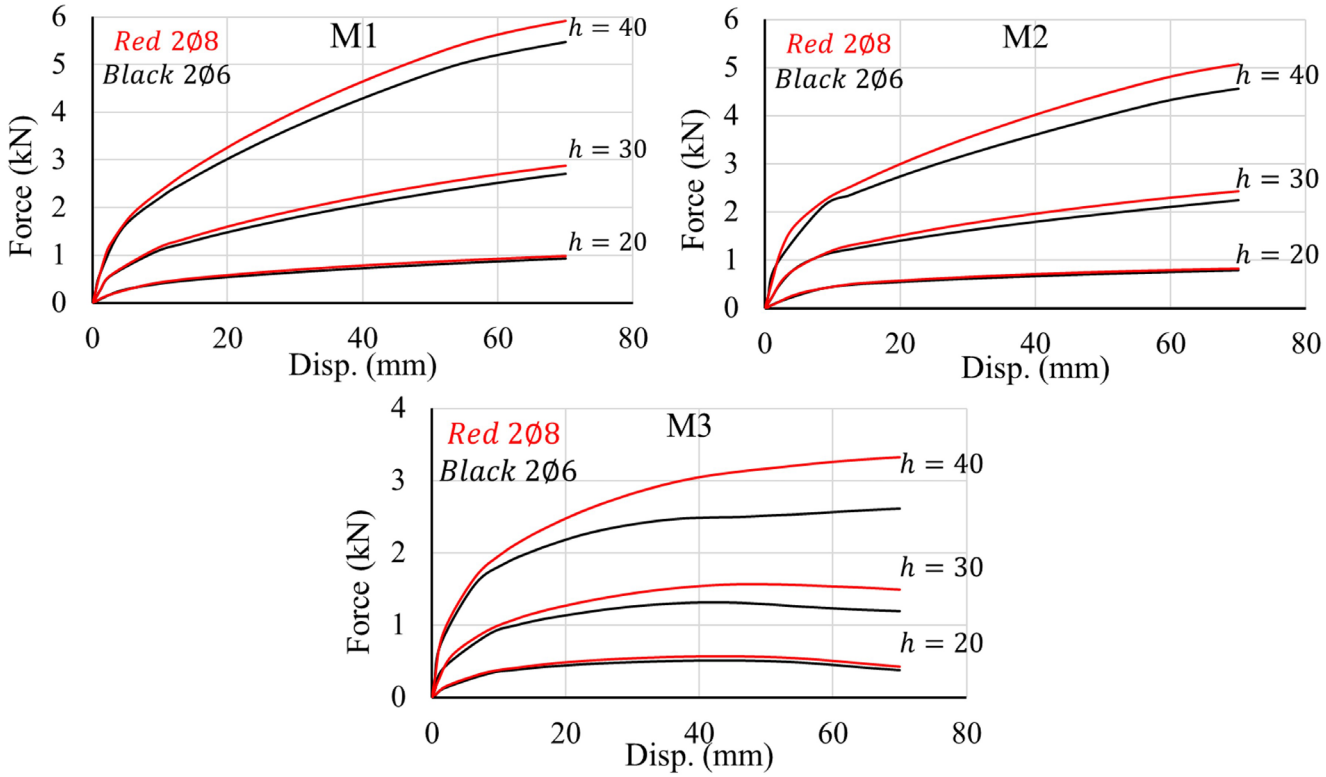


**Fig. 14** Results of HPFRCC models

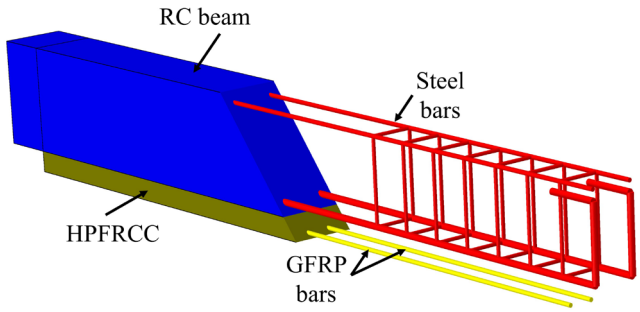


**Fig. 15** Details of the parametric model

Fig. 17 (a) and (b) illustrates the normalized strength and normalized stiffness of the parametric models plotted against $\alpha$, respectively. In Fig. 17 (a) and (b), the vertical axis represents results normalized to the original beam. It is evident from both results that they are directly dependent on $\alpha$. The M1 models exhibit the highest strength, boasting an increase of 80% compared to the OB. Furthermore, models M1 and M2 display similar stiffness results. Notably, the maximum stiffness is four times that of the OB, underscoring that reinforcing the beam has a more pronounced impact on its stiffness than its strength. Since the Young's modulus of GFRP bars is higher than that of HPFRCC and these members are positioned at a considerable distance from the neutral axis, they significantly influence the moment of inertia and, consequently, the stiffness of the section.

Stiffness plays a critical role in evaluating the durability of reinforced concrete structures, which is determined through displacement, crack shape, and crack length measurements. The relative stiffness percentage of reinforced concrete beams that have undergone strengthening can be assessed by analyzing the force-displacement curve at the service load and 90% of the original beam's $P_{max}$ [1].

$$\text{Relative Stiffness}(\%) = 100\left(\frac{\Delta_{OB} - \Delta_{SB}}{\Delta_{OB}}\right) \tag{7}$$

In Eq. (7), $\Delta_{OB}$ and $\Delta_{SB}$ represent the deflections of the original and strengthened beams, respectively. According to ACI 318-95 [42], the service load is defined as the amount of load corresponding to a deflection equal to $L/480$ (where $L$ is the beam length). The results of relative stiffness are presented in Fig. 18. It is evident that these results are directly correlated with the height of the HPFRCC, with an incremental effect observed with increasing GFRP diameter.

In the service load results (Fig. 18 (a)), the M2 models exhibited the highest relative stiffness, while the lowest relative stiffness was observed for the M3 model. Conversely, in the results obtained at 90% of the maximum load (Fig. 18 (b)), the relative stiffness of the M1 and M2 models was nearly identical, while the M3 model exhibited the lowest relative stiffness.

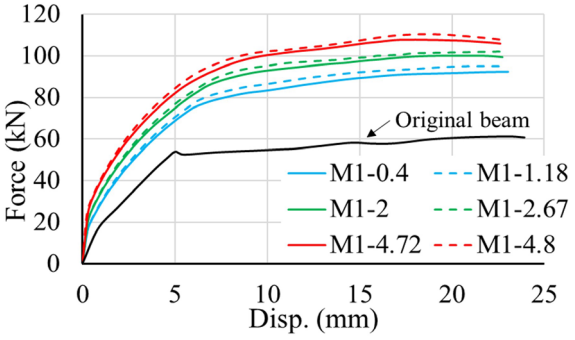


(a)

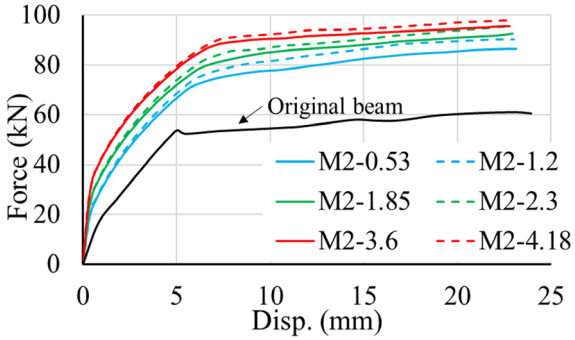


(b)

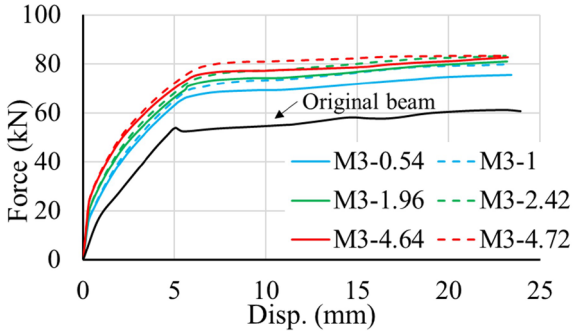


(c)

**Fig. 16** The force-displacement results of strengthened beams

The total energy dissipation (ED) capacity of the models was determined by calculating the area under their force-displacement curves, representing the work of toughness or rupture. Fig. 19 illustrates the ED values for all numerical models. In Fig. 19, the vertical axis presents the results of ED normalized to the OB, which was calculated as 1251 J based on Fig. 11 (a). The horizontal axis depicts the height of the HPFRCC. The strengthened beams exhibit a greater ED capability compared to the original beam. Notably, Model M1 demonstrated the highest ED, particularly with a GFRP diameter of 8 mm and an HPFRCC height of 40 mm, showcasing a 70% increase in ED compared to the original beam.

The variables considered for the main models in this study for the strengthening of RC beams include the increase in the diameter of GFRP and the height of HPFRCC.

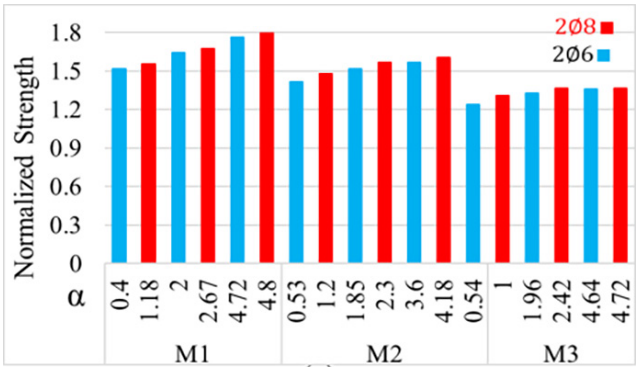


(a)

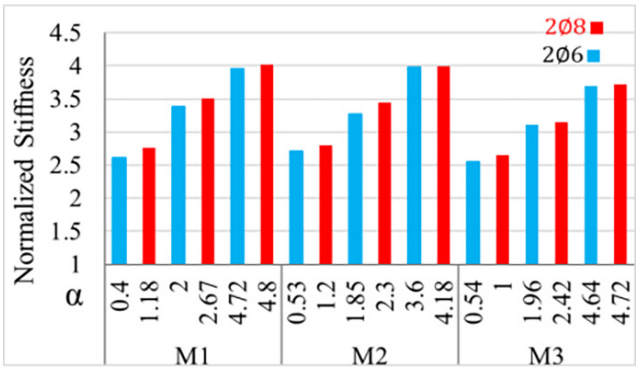


(b)

**Fig. 17** The results of parametric studies (a) normalized strength and (b) normalized stiffness

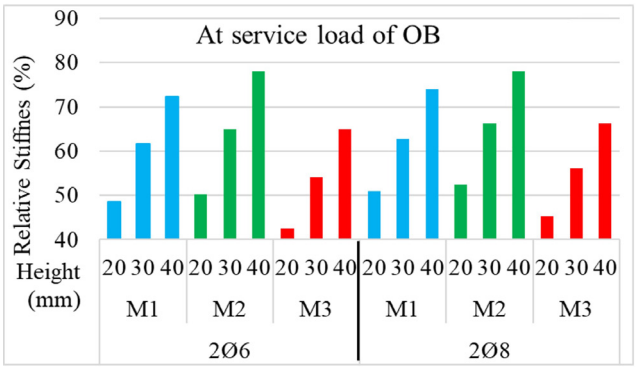


(a)

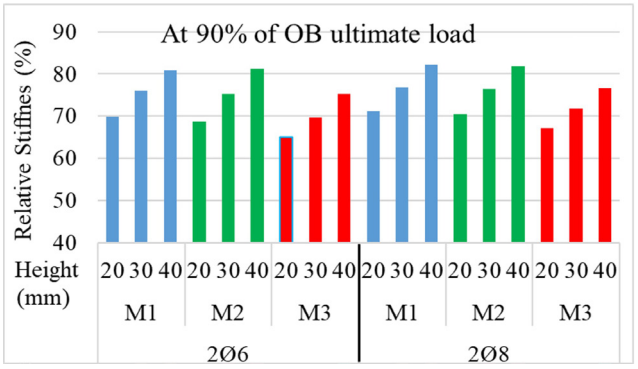


(b)

**Fig. 18** The result of relative stiffness for (a) at service load (b) at 90% of the ultimate load of OB

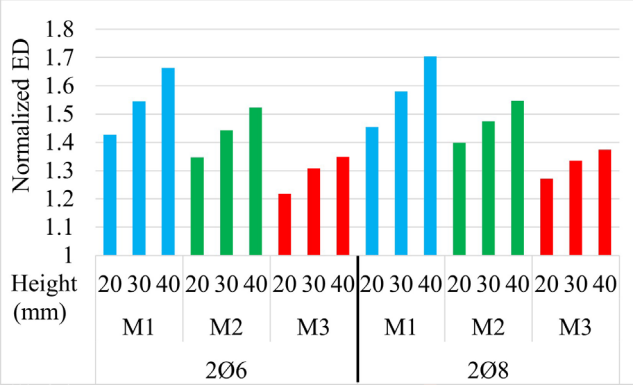


**Fig. 19** The results of the energy dissipation capacity of the models

If, depending on the conditions, a low-height HPFRCC is used for strengthening a beam, the recommended solution is to increase the diameter of the GFRP. The results of this study demonstrate that increasing the diameter of the GFRP and the height of the HPRCC can enhance stiffness, strength, and energy absorption. Therefore, the height and diameter of the GFRP can be determined based on the specific conditions of each structure.

## 5 Conclusions

This research explored the impact of RC beams reinforced with prefabricated concrete reinforcement plates. Initially, nine test specimens were employed to examine the influence of various steel fibers (micro steel, polyvinyl alcohol, and macro steel) as well as GFRP bars on the flexural behavior of HPFRCC. These experimental models were tested both with and without GFRP bars and with lengths of 500 and 1700 mm. Subsequently, four-point bending tests were conducted, and the force-displacement outputs were analyzed. Following this, the nine experimental models were calibrated using ABAQUS software, and validation was carried out with an RC beam sample. Numerical analysis was then performed to assess the effect of HPFRCC height and GFRP diameter on their respective force-displacement diagrams. In the latter part of the study, parametric analyses were conducted to explore the influence of HPFRCC height and GFRP rebar diameter on the behavior of RC beams strengthened with these plates. The number of experimental samples was 9, and the number of numerical models was 36. The results obtained from this model encompassed elastic and relative stiffness, energy dissipation, and ultimate strength. The summarized findings from these analyses are detailed in the subsequent paragraphs:

- The experimental force-displacement diagram results indicated that among the samples lacking GFRP bars, the M3 model exhibited the highest strength, while among the samples with GFRP bars, it demonstrated the lowest strength.
- The force-displacement results of the experimental samples lacking GFRP bars indicated that in the M3 and M2 types, the strength decreased at a deflection of 3 mm, while in the M1 sample, it decreased at a deflection of 2 mm. However, for samples with a length of 1700 mm, both M1 and M2 retained their strength until the completion of loading, whereas M3 experienced a decline in strength after the deflection increased to 38 mm.
- The results related to the ultimate strength and elastic stiffness of the reinforced RC beam exhibited a direct correlation with the stiffness ratio of HPFRCC to the original beam. Notably, the strengthened beam of type M1 demonstrated the highest ultimate strength. Moreover, the elastic stiffness results for the strengthened beam in both M1 and M2 modes were nearly identical. Specifically, in a model featuring a 40 mm HPFRCC height and 8 mm GFRP bar diameter, the ultimate strength and elastic stiffness of the RC beam increased by 1.8 and 4 times, respectively.
- The relative stiffness of the concrete beam exhibited a direct correlation with its HPFRCC height, with minimal influence from the diameter of the GFRP bar. Additionally, types M1 and M2 yielded nearly identical results, both surpassing those of M3.
- The strengthened beam exhibited greater energy dissipation compared to the original beam. The most significant factor influencing the energy dissipation results was the height of HPFRCC; an increase in its height correlated with higher energy dissipation in the model. Specifically, the M1 model demonstrated a 70% increase in energy dissipation compared to the original beam, particularly with an HPFRCC height of 40 mm and a GFRP rebar diameter of 8 mm.

## References

[1] Alharthi, Y. M., Emara, M., Elamary, A. S., Sharaky, I. A. "Flexural response and load capacity of reinforced concrete beams strengthened with reinforced mortar layer", Engineering Structures, 245, 112884, 2021. https://doi.org/10.1016/j.engstruct.2021.112884

[2] Ünal, A., Cengiz, S., Kamanlı, M. "Effect of Stirrup Spacing, Polypropylene Fiber Ratio on Behavior of Reinforced Concrete Beams", Periodica Polytechnica Civil Engineering, 65(2), pp. 522–536, 2021. https://doi.org/10.3311/PPci.16802

[3] Abdesselam, A., Merdas, A., Fiorio, B., Chikh, N.-E. "Experimental and Numerical Study on RC Beams Strengthened by NSM Using CFRP Reinforcements", Periodica Polytechnica Civil Engineering, 67(4), pp. 1214–1233, 2023. https://doi.org/10.3311/PPci.21309

[4] Ranković, S., Folić, R., Zorić, A., Vacev, T., Petrović, Ž., Kovačević, D. "Experimental Analysis of an Innovative Double Strap Joint Splicing of GFRP Bars by NSM Methods for Strengthening RC Beams", Periodica Polytechnica Civil Engineering, 68(1), pp. 185–196, 2024. https://doi.org/10.3311/PPci.22681

[5] Barham, W. S., Obaidat, Y. T., Al-Maabreh, A. I. "Effect of Aggregate Size on the Bond Behavior between Carbon Fiber–Reinforced Polymer Sheets and Concrete", Journal of Materials in Civil Engineering, 31(12), 04019295, 2019. https://doi.org/10.1061/(ASCE)MT.1943-5533.0002950

[6] Papanicolaou, C. G., Triantafillou, T. C., Papathanasiou, M., Karlos, K. "Textile reinforced mortar (TRM) versus FRP as strengthening material of URM walls: out-of-plane cyclic loading", Materials and Structures, 41(1), pp. 143–157, 2008. https://doi.org/10.1617/s11527-007-9226-0

[7] Tetta, Z. C., Koutas, L. N., Bournas, D. A. "Textile-reinforced mortar (TRM) versus fiber-reinforced polymers (FRP) in shear strengthening of concrete beams", Composites Part B: Engineering, 77, pp. 338–348, 2015. https://doi.org/10.1016/j.compositesb.2015.03.055

[8] Smith, A. S. J., Xu, G. "Simplified, Cost-Effective Method of Studying the Effect of Steel Fibers on Ultra-high Performance Concrete Specimens' Properties/Members' Performance", Periodica Polytechnica Civil Engineering, 67(1), pp. 308–324, 2023. https://doi.org/10.3311/PPci.20833

[9] Mahdi, A. M. "Impact of Failure-surface Parameters of Concrete Damage Plasticity Model on the Behavior of Reinforced Ultra-high Performance Concrete Beams", Periodica Polytechnica Civil Engineering, 67(2), pp. 495–504, 2023. https://doi.org/10.3311/PPci.21345

[10] Osama, B., Sakr, M. "Modeling of Ultra-high Performance Fiber Reinforced Concrete Filled Steel Tube Columns under Eccentric Loading", Periodica Polytechnica Civil Engineering, 67(1), pp. 10–23, 2023. https://doi.org/10.3311/PPci.20593

[11] Al-Osta, M. A., Isa, M. N., Baluch, M. H., Rahman, M. K. "Flexural behavior of reinforced concrete beams strengthened with ultra-high performance fiber reinforced concrete", Construction and Building Materials, 134, pp. 279–296, 2017. https://doi.org/10.1016/j.conbuildmat.2016.12.094

[12] Naser, M. Z., Hawileh, R. A., Abdalla, J. "Modeling Strategies of Finite Element Simulation of Reinforced Concrete Beams Strengthened with FRP: A Review", Journal of Composites Science, 5(1), 19, 2021. https://doi.org/10.3390/jcs5010019

[13] Said, A., Elsayed, M., El-Azim, A. A., Althoey, F., Tayeh, B. A. "Using ultra-high performance fiber reinforced concrete in improvement shear strength of reinforced concrete beams", Case Studies in Construction Materials, 16, e01009, 2022. https://doi.org/10.1016/j.cscm.2022.e01009

[14] Folino, P., Ripani, M., Xargay, H., Rocca, N. "Comprehensive analysis of Fiber Reinforced Concrete beams with conventional reinforcement", Engineering Structures, 202, 109862, 2020. https://doi.org/10.1016/j.engstruct.2019.109862

[15] Abadel, A., Abbas, H., Almusallam, T., Alshaikh, I. M. H., Khawaji, M., Alghamdi, H., Salah, A. A. "Experimental study of shear behavior of CFRP strengthened ultra-high-performance fiber-reinforced concrete deep beams", Case Studies in Construction Materials, 16, e01103, 2022. https://doi.org/10.1016/j.cscm.2022.e01103

[16] Bui, T. T., Nana, W. S. A., Doucet-Ferru, B., Bennani, A., Lequay, H., Limam, A. "Shear Performance of Steel Fiber Reinforced Concrete Beams Without Stirrups: Experimental Investigation", International Journal of Civil Engineering, 18(8), pp. 865–881, 2020. https://doi.org/10.1007/s40999-020-00505-8

[17] Zhang, W., Kang, S., Huang, Y., Liu, X. "Behavior of Reinforced Concrete Beams without Stirrups and Strengthened with Basalt Fiber–Reinforced Polymer Sheets", Journal of Composites for Construction, 27(2), 04023007, 2023. https://doi.org/10.1061/JCCOF2.CCENG-4082

[18] Yu, Y., Zhao, X.-Y., Xu, J.-J., Wang, S.-C., Xie, T.-Y. "Evaluation of Shear Capacity of Steel Fiber Reinforced Concrete Beams without Stirrups Using Artificial Intelligence Models", Materials, 15(7), 2407, 2022. https://doi.org/10.3390/ma15072407

[19] Alshboul, O., Almasabha, G., Shehadeh, A., Mamlook, R. E. A., Almuflih, A. S., Almakayeel, N. "Machine Learning-Based Model for Predicting the Shear Strength of Slender Reinforced Concrete Beams without Stirrups", Buildings, 12(8), 1166, 2022. https://doi.org/10.3390/buildings12081166

[20] Liu, S., Cao, S., Hao, Y., Chen, P., Ma, G. "Prediction models of compressive mechanical properties of steel fiber-reinforced cementitious composites (SFRCC)", Journal of Building Engineering, 84, 108629, 2024. https://doi.org/10.1016/j.jobe.2024.108629

[21] Liao, J., Zeng, J.-J., Zheng, Y., Liu, Y., Zhuge, Y., Zhang, L. "Constitutive models of ultra-high performance concrete (UHPC) under true tri-axial compression and an analysis-oriented model for FRP-confined UHPC", Engineering Structures, 305, 117656, 2024. https://doi.org/10.1016/j.engstruct.2024.117656

[22] Zhang, S. S., Wang, J. J., Lin, G., Yu, T., Fernando, D. "Stress-strain models for ultra-high performance concrete (UHPC) and ultra-high performance fiber-reinforced concrete (UHPFRC) under triaxial compression", Construction and Building Materials, 370, 130658, 2023. https://doi.org/10.1016/j.conbuildmat.2023.130658

[23] Yokota, H., Rokugo, K., Sakata, N. "JSCE recommendations for design and construction of high performance fiber reinforced cement composite with multiple fine cracks", In: High performance fiber reinforced cement composites, vol. 2, Springer, Tokyo, Japan, 2008.

[24] Zhu, M., Zhang, J., Chen, B., Wu, M., Han, J. "Numerical simulation of cost-effective green high-ductility engineered cementitious composites based on meso-scale particle flow model", Construction and Building Materials, 356, 128973, 2022. https://doi.org/10.1016/j.conbuildmat.2022.128973

[25] Dadmand, B., Pourbaba, M., Riahi, R. "Experimental and Numerical Investigation of Different Types of Jacketing Effect on Retrofitting RC Short Columns Using ECC Concrete", Periodica Polytechnica Civil Engineering, 66(2), pp. 603–613, 2022. https://doi.org/10.3311/PPci.19114

[26] Solhmirzaei, R., Kodur, V. "A Numerical Model for Tracing Structural Response of Ultra-High Performance Concrete Beams", Modelling, 2(4), pp. 448–466, 2021. https://doi.org/10.3390/modelling2040024

[27] Cao, M., Liu, Z., Xie, C. "Effect of steel-PVA hybrid fibers on compressive behavior of $CaCO_3$ whiskers reinforced cement mortar", Journal of Building Engineering, 31, 101314, 2020. https://doi.org/10.1016/j.jobe.2020.101314

[28] Tan, G., Zhu, Z., Wang, W., He, X. "A fractal-based approach for cracking characterization and whole process prediction exploration of PP fiber reinforced ECC containing sustainable ingredients", Construction and Building Materials, 318, 126015, 2022. https://doi.org/10.1016/j.conbuildmat.2021.126015

[29] ASTM "ASTM C305-13 Standard Practice for Mechanical Mixing of Hydraulic Cement Pastes and Mortars of Plastic Consistency", ASTM International, West Conshohocken, PA, USA, 2013. https://doi.org/10.1520/C0305-13

[30] Tanarslan, H. M., Alver, N., Jahangiri, R., Yalçınkaya, Ç., Yazıcı, H. "Flexural strengthening of RC beams using UHPFRC laminates: Bonding techniques and rebar addition", Construction and Building Materials, 155, pp. 45–55, 2017. https://doi.org/10.1016/j.conbuildmat.2017.08.056

[31] Hibbitt, Karlsson & Sorensen, Inc. "ABAQUS/CAE User's Manual", Hibbitt, Karlsson & Sorensen, Inc., Pawtucket, RI, USA, 2000.

[32] Huang, B.-T., Li, Q.-H., Xu, S.-L., Zhang, L. "Static and fatigue performance of reinforced concrete beam strengthened with strain-hardening fiber-reinforced cementitious composite", Engineering Structures, 199, 109576, 2019. https://doi.org/10.1016/j.engstruct.2019.109576

[33] Cheraghi, K., TahamouliRoudsari, M., Kiasat, S., Cheraghi, K. "Numerical and analytical investigation of cyclic behavior of D-Shape yielding damper", Structural Engineering and Mechanics, 89(4), pp. 411–420, 2024. https://doi.org/10.12989/sem.2024.89.4.411

[34] Cheraghi, K., TahamouliRoudsari, M., Kiasat, S. "Numerical and analytical investigation of U-shape dampers and its effect on steel frames", Structures, 55, pp. 498–509, 2023. https://doi.org/10.1016/j.istruc.2023.06.037

[35] BSI "BS EN 1992-1-1:2004 Eurocode 2: Design of concrete structures – Part 1-1: General rules and rules for buildings", BSI, London, UK, 2004.

[36] Cheraghi, K., TahamouliRoudsari, M., Kiasat, S., Cheraghi, K. "Numerical study of metallic dampers' effect on seismic performance of concrete frames", Asian Journal of Civil Engineering, 25(3), pp. 2431–2441, 2024. https://doi.org/10.1007/s42107-023-00917-6

[37] Cheraghi, K., Darbandkohi, M., TahamouliRoudsari, M., Kiasat, S. "Seismic behavior of RC frames with partially attached steel shear walls: A numerical study", Earthquakes and Structures, 25(6), pp. 443–454, 2023. https://doi.org/10.12989/eas.2023.25.6.443

[38] Cheraghi, K., Tavana, M. H., Aghayari, R. "Investigating the Effect of Low-Yield Yielding Dampers on the Seismic Behavior of Steel Frames", Periodica Polytechnica Civil Engineering, 67(3), pp. 925–935, 2023. https://doi.org/10.3311/PPci.21804

[39] Cheraghi, K., TahamouliRoudsari, M., Kiasat, S., Esfandiari, J. "Numerical Investigation of Cyclic Behavior of Angled U-shaped Yielding Damper on Steel Frames", Periodica Polytechnica Civil Engineering, 68(2), pp. 426–434, 2024. https://doi.org/10.3311/PPci.23213

[40] Raza, A., Khan, Q. u. Z., Ahmad, A. "Numerical Investigation of Load-Carrying Capacity of GFRP-Reinforced Rectangular Concrete Members Using CDP Model in ABAQUS", Advances in Civil Engineering, 2019, 1745341, 2019. https://doi.org/10.1155/2019/1745341

[41] Raza, A., Rafique, U. "Efficiency of GFRP bars and hoops in recycled aggregate concrete columns: Experimental and numerical study", Composite Structures, 255, 112986, 2021. https://doi.org/10.1016/j.compstruct.2020.112986

[42] ACI Committee 318 "Building Code Requirements for Structural Concrete (ACI 318-95) and Commentary (ACI 318R-95), American Concrete Institute, Farmington Hills, MI, USA, 1995.

## Appendix

The Tables A1–A5 show the material properties of concrete in tension and compression for the beam model, as well as the HPFRCC properties for the numerical model.

The material properties of the RC beam for the numerical model are provided in Tables A3 and A4.

**Table A1** Compressive strength of HPFRCC (numerical model)

| | Compressive behavior | | |
|---|---|---|---|
| | M1 | M2 | M3 |
| Inelastic strain | Yield stress (MPa) | Yield stress (MPa) | Yield stress (MPa) |
| 0 | 44.01 | 35.11 | 43.84 |
| 0.00025 | 51.56 | 42.64 | 51.32 |
| 0.0005 | 58.63 | 49.65 | 58.31 |
| 0.00075 | 65.17 | 56.1 | 64.77 |
| 0.001 | 71.16 | 61.98 | 70.66 |
| 0.00125 | 76.54 | 67.26 | 75.94 |
| 0.0015 | 81.26 | 71.93 | 80.57 |
| 0.00175 | 85.28 | 75.95 | 84.5 |
| 0.002 | 88.54 | 79.31 | 87.67 |
| 0.00225 | 90.96 | 81.97 | 90.03 |
| 0.0025 | 92.47 | 83.91 | 91.49 |
| 0.00275 | 93 | 85.1 | 92 |
| 0.003 | 92.44 | 85.5 | 91.46 |
| 0.00325 | 90.69 | 85.09 | 89.79 |
| 0.0035 | 87.63 | 83.82 | 86.87 |
| 0.00375 | 83.13 | 81.66 | 82.6 |

**Table A2** Tensile behavior of HPFRCC (numerical model)

| | Tensile behavior | | |
|---|---|---|---|
| | M1 | M2 | M3 |
| Cracking strain | Yield stress (MPa) | Yield stress (MPa) | Yield stress (MPa) |
| 0 | 6.9 | 6.5 | 5.7 |
| 0.00025 | 10.25 | 9.83 | 9.54 |
| 0.0005 | 9.13 | 8.32 | 7.31 |
| 0.00075 | 8.17 | 7.12 | 5.82 |
| 0.001 | 7.35 | 6.15 | 4.74 |
| 0.00125 | 6.64 | 5.34 | 3.93 |
| 0.0015 | 6.02 | 4.66 | 3.3 |
| 0.00175 | 5.47 | 4.09 | 2.8 |
| 0.002 | 4.98 | 3.59 | 2.38 |
| 0.00225 | 4.54 | 3.15 | 2.04 |
| 0.0025 | 4.15 | 2.77 | 1.64 |
| 0.00275 | 3.79 | 2.43 | 1.33 |
| 0.003 | 3.46 | 2.13 | 1.07 |

**Table A3** Tensile and compressive behavior of the RC beam

| Compressive behavior | | Tensile behavior | |
|---|---|---|---|
| Inelastic strain | Yield stress (MPa) | Cracking strain | Yield stress (MPa) |
| 0 | 25.32 | 0 | 5 |
| 0.00025 | 31.97 | 0.00025 | 3.82 |
| 0.0005 | 37.65 | 0.0005 | 3.18 |
| 0.00075 | 42.32 | 0.00075 | 2.77 |
| 0.001 | 45.93 | 0.001 | 2.5 |
| 0.00125 | 48.43 | 0.00125 | 2.29 |
| 0.0015 | 49.78 | 0.0015 | 2.14 |
| 0.00175 | 49.9 | 0.00175 | 2.02 |
| 0.002 | 48.74 | 0.002 | 1.92 |
| 0.00225 | 46.24 | 0.00225 | 1.84 |
| 0.0025 | 42.32 | 0.0025 | 1.77 |
| 0.00275 | 36.92 | 0.00275 | 1.71 |
| 0.003 | 29.94 | 0.003 | 1.66 |
| 0.00325 | 21.31 | 0.00325 | 1.62 |
| 0.0035 | 13.21 | 0.0035 | 1.58 |

**Table A4** Concrete material properties (RC beam)

| Parameter | Value |
|---|---|
| Density of concrete (kg/m$^3$) | 2400 |
| Poisson's ratio | 0.2 |
| Young's modulus (GPa) | 37 |

**Table A5** Reinforcement properties

| Longitudinal | | Stirrups | |
|---|---|---|---|
| Plastic strain | Yield stress (MPa) | Plastic strain | Yield stress (MPa) |
| 0 | 386 | 0 | 280 |
| 0.038 | 572 | 0.038 | 480 |